The University of Texas ARLINGTON

MATHEMATICS
Preprint Series

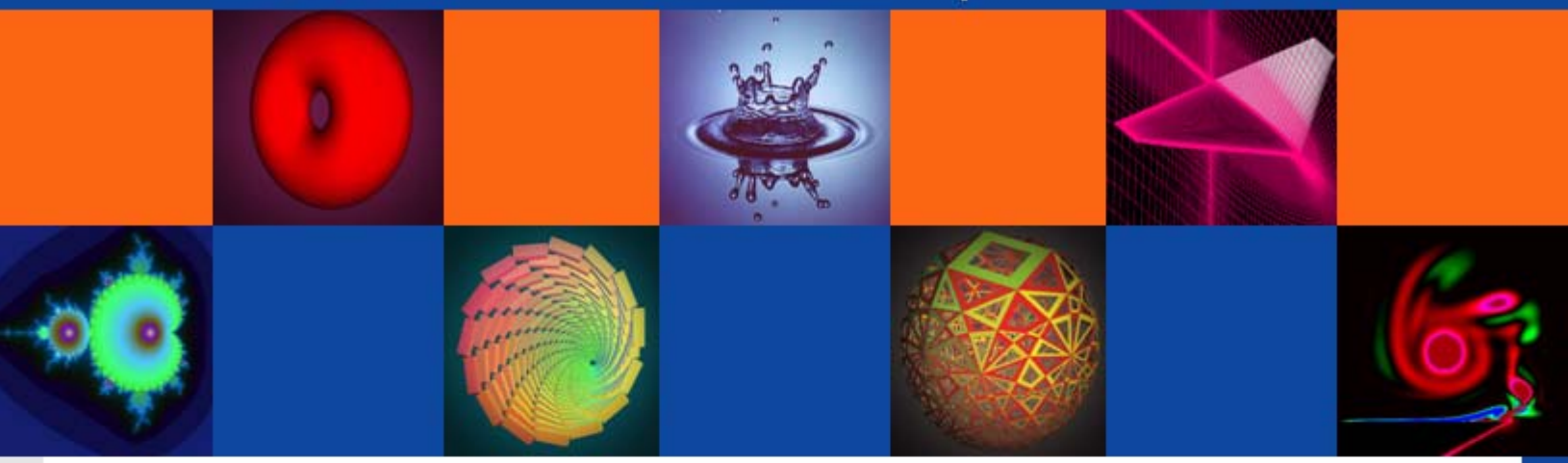

Numerical Study of Passive and Active Flow Separation Control Over a NACA0012 Airfoil

H. Shan, L. Jiang, C. Liu, M. Love, B. Marines

Technical Report 2007-03

http://www.uta.edu/math/preprint/

Numerical Study of Passive and Active Flow Separation Control over a NACA0012 Airfoil

Hua Shan[1] *, Li Jiang[2], Chaoqun Liu[3]
University of Texas at Arlington, Arlington TX 76019

and

Michael Love[4], Brant Maines[5]
Lockheed Martin Aeronautics Company, Fort Worth, TX 76101

Abstract

This paper is focused on numerical investigation of subsonic flow separation over a NACA0012 airfoil with a 6° angle of attack and flow separation control with vortex generators. The numerical simulations of three cases including an uncontrolled baseline case, a controlled case with passive vortex generator, and a controlled case with active vortex generator were carried out. The numerical simulation solves the three-dimensional Navier-Stokes equations for compressible flow using a fully implicit LU-SGS method. A fourth-order finite difference scheme is used to compute the spatial derivatives. The immersed boundary method is used to model both the passive and active vortex generators. The characteristic frequency that dominates the flow is the natural frequency of separation in the baseline case. The introduction of the passive vortex generator does not alter the frequency of separation. In the case with active control, the frequency of the sinusoidal forcing was chosen close to the natural frequency of separation. The time- and spanwise-averaged results were used to examine the mean flow field for all three cases. The passive vortex generators can partially eliminate the separation by reattaching the separated shear layer to the airfoil over a significant extent. The size of the averaged separation zone has been reduced by more than 80%. The flow control with active vortex generator is more effective and the separation zone is not visible in the averaged results. The three-dimensional structures of the flow field have also been studied.

[1] Assistant Professor, Department of Mathematics. * Corresponding author. 817-272-5685, E-mail: hshan@uta.edu.
[2] Research Scientist, Department of Mathematics
[3] Professor, Department of Mathematics
[4] Engineer Senior Staff
[5] Aerospace Engineering Senior Staff

Keywords: flow separation, passive and active control, vortex generator, direct numerical simulation

1. Introduction

At low Reynolds number, the boundary layer on the upper surface of an airfoil at incidence remains laminar at the onset of pressure recovery. As laminar flow is less resistant to an adverse pressure gradient, flow separation may occur near the leading edge of the airfoil. The separated shear layer is inviscidly unstable and vortices are formed due to the Kelvin-Helmholtz mechanism [1]. The detached shear layer may also undergo rapid transition to turbulence and the separated flow may reattach to the wall surface because of the increased entrainment associated with the turbulent flow [11] and form an attached turbulent boundary layer. The formation of the separation bubble depends on the Reynolds number, the pressure distribution, the surface curvature, and freestream turbulence level. The location and the extent of flow separation could directly affect the airfoil performance or the efficiency of the turbo-machinery. The flow separation over a wing in flight results in the loss of lift and increase of drag as well as generation of aerodynamic noise.

Flow control through boundary layer manipulation to prevent or postpone separation can significantly reduce the pressure drag, enhance the lift, and improve the performance of the aircraft. Traditionally, flow separation control is implemented through airfoil shaping, surface cooling, moving walls, tripping early transition to turbulence, and near-wall momentum addition. Given an imposed pressure field, the kernel in separation postponement is to add momentum to the very near-wall region [11].

Among the near-wall momentum addition methods, steady or pulsed blowing jets and vortex generators (VG) have been widely used. The experiments conducted by Bons et al. [6] have shown that steady Vortex Generator Jets (VGJ) have the effect of reducing or entirely eliminating the separation zone on the suction surface of the blade at low Reynolds number, while the pulsed VGJs produce a comparable improvement to that for steady VGJs but with an order of magnitude less required mass-flow. In contrast to

steady blowing, the oscillatory blowing takes advantage of inherent local instabilities in the nearwall shear layer that causes the selective amplification of the input oscillation frequency. These amplified disturbances convect downstream along the airfoil as coherent large structures that serve to mix the boundary layer flow and delay separation [25]. A comprehensive review of flow separation control by periodic excitation in various forms including hydrodynamic, acoustic, and blowing/suction methods, can be found in [14]. The conventional passive vortex generator was first developed by Taylor [36] in 1947 to prevent boundary-layer separation in wind tunnel diffuser. The first systematic study of vortex generations and their effects on the boundary-layer was performed by Schubauer and Spangenberg [30] in late 1950's. Since then the vortex generators have been successfully applied to lifting surfaces in many aeronautical applications for control of flow separation and reduction of drag in a turbulent boundary layer [7, 16, 20]. The vortices created by vortex generators transfer low energy fluid from the surface into the mainstream, and bring higher energy fluid from the mainstream down to the surface where the higher kinetic energy level is able to withstand a greater pressure rise before separation occurs. Another mechanism introduced by the vortex generator is associated with the excitation of the local instability waves that lead to an early transition to turbulence, which delays the flow separation and reduces the size of the separation zone.

Generally, vortex generators are designed as either passive or active devices. The effectiveness of a passive vortex generator, whose size, position, and orientation are fixed on the surface, is limited to a narrow operational range. Lin [21] gave an in-depth review of boundary layer flow separation control by the passive low-profile vortex generators. More recently, Godard et al. [12] conducted an experimental study to optimize the standard passive vane-type vortex generators over of bump in a boundary layer wind tunnel, which mimics the adverse pressure gradient on the suction side of an airfoil at the verge of separation. Two types of VG configurations that produce co- and counter-rotating longitudinal vortices were tested, and the counter-rotating device appears to be more effective. On the other hand, the active vortex generator, developed from the concept of dynamic flow control is capable of changing its size, position, and orientation according to different flow conditions. The basic experimental studies of Shizawa and Mizusaki have revealed the response of flow behind the active vortex generators over a

flat plate [34, 35]. Other experimental research has also shown that the active control using deployable vortex generators enhances the momentum mixing and energizes the boundary layer so that the flow separations is delayed [27]. It is also interesting to find experimentally that the high-frequency deployable micro vortex generator system (HiMVG) producing an oscillatory flow field at frequencies ranging from 30 to 70 Hz is very effective in mitigating flow separation on the upper surface of a deflected flap [26]. However, the mechanism of flow control with active vortex generators is still unclear due to lack of systematic studies.

In cases of flow separation, instability and laminar-turbulent transition may take place in the detached free shear layer. It is widely accepted that the instability in the separation zone is driven by the Kelvin-Helmholtz mechanism if the disturbance level of freestream is low. In this case, transition takes place due to nonlinear breakdown of spatially growing traveling waves in the separated free shear layer [37]. When the shear layer becomes turbulent, the detached shear layer may reattach to the surface, creating a separation bubble and forming an attached turbulent boundary layer. Yarusevych et al. [40] studied the boundary layer separation on a NACA0025 airfoil via hot-wire anemometry and surface pressure measurements and found the fundamental frequency associated with flow separation.

Flow transition in separation bubbles is a classic topic which has been studied both theoretically and numerically for many years [5]. Among the different approaches used for the study of flow instability, there are the linear stability theory (LST) [9], the parabolized stability equations (PSE) method [4], and direct numerical simulation (DNS) and large eddy simulation (LES). LST is mainly a local analysis with assumption of parallel base flow. PSE assumes a steady base flow with no elliptic part. These assumptions do not apply for the case of flow separation and transition around an incident airfoil. With the development of computer resources and efficient numerical methods, high resolution and high accuracy DNS/LES has become feasible for the study of transition in separated flows and flow separation control. Early efforts of the authors include the numerical simulations of two-dimensional flow separation, three-dimensional separation and transition over a NACA0012 airfoil with 4° angle of attack [31,32], flow

separation control on a NACA0012 airfoil with pulsed blowing jets [19], and numerical simulation of flow behind a pair of active vortex generators over a flat plate [33].

The objective of current work is to study the feasibility of simulating the flow separation control with vortex generators using a technique that combines the body-fitted mesh for the airfoil in a curvilinear coordinate system and the immersed boundary method for modeling the vortex generator. Direct numerical simulations of the following three cases were performed on a NACA0012 airfoil at 6° angle of attack: 1) uncontrolled flow separation (baseline case); 2) flow control with passive vortex generators (Case 1); and 3) flow control with active vortex generators (Case 2). The organization of the remaining part of this paper is as follows. In Section 2, we briefly introduce the mathematical model and numerical methods. Section 3 presents the layout of the vortex generators and problem formulations for the baseline case, and the two controlled cases. Section 4 shows the numerical results for all three cases. Conclusions are given in Section 5.

2. Mathematical Model and Numerical Methods

2.1 *Governing Equations*

The three-dimensional compressible Navier-Stokes equations in generalized curvilinear coordinates (ξ, η, ζ) are written in conservative form as

$$\frac{1}{J}\frac{\partial Q}{\partial t}+\frac{\partial\left(E-E_v\right)}{\partial \xi}+\frac{\partial\left(F-F_v\right)}{\partial \eta}+\frac{\partial\left(G-G_v\right)}{\partial \zeta}=0$$

The vector of conserved quantities Q, inviscid flux vector (E, F, G), and viscous flux vector (E_v, F_v, G_v) are defined by

$$Q=\begin{pmatrix}\rho\\ \rho u\\ \rho v\\ \rho w\\ E_t\end{pmatrix},\quad E=\frac{1}{J}\begin{pmatrix}\rho U\\ \rho U u+p\xi_x\\ \rho U v+p\xi_y\\ \rho U w+p\xi_z\\ U\left(E_t+p\right)\end{pmatrix},\quad F=\frac{1}{J}\begin{pmatrix}\rho V\\ \rho V u+p\eta_x\\ \rho V v+p\eta_y\\ \rho V w+p\eta_z\\ V\left(E_t+p\right)\end{pmatrix},\quad G=\frac{1}{J}\begin{pmatrix}\rho W\\ \rho W u+p\zeta_x\\ \rho W v+p\zeta_y\\ \rho W w+p\zeta_z\\ W\left(E_t+p\right)\end{pmatrix},$$

$$E_v = \frac{1}{J}\begin{pmatrix} 0 \\ \tau_{xx}\xi_x + \tau_{yx}\xi_y + \tau_{zx}\xi_z \\ \tau_{xy}\xi_x + \tau_{yy}\xi_y + \tau_{zy}\xi_z \\ \tau_{xz}\xi_x + \tau_{yz}\xi_y + \tau_{zz}\xi_z \\ Q_x\xi_x + Q_y\xi_y + Q_z\xi_z \end{pmatrix}, F_v = \frac{1}{J}\begin{pmatrix} 0 \\ \tau_{xx}\eta_x + \tau_{yx}\eta_y + \tau_{zx}\eta_z \\ \tau_{xy}\eta_x + \tau_{yy}\eta_y + \tau_{zy}\eta_z \\ \tau_{xz}\eta_x + \tau_{yz}\eta_y + \tau_{zz}\eta_z \\ Q_x\eta_x + Q_y\eta_y + Q_z\eta_z \end{pmatrix}, G_v = \frac{1}{J}\begin{pmatrix} 0 \\ \tau_{xx}\zeta_x + \tau_{yx}\zeta_y + \tau_{zx}\zeta_z \\ \tau_{xy}\zeta_x + \tau_{yy}\zeta_y + \tau_{zy}\zeta_z \\ \tau_{xz}\zeta_x + \tau_{yz}\zeta_y + \tau_{zz}\zeta_z \\ Q_x\zeta_x + Q_y\zeta_y + Q_z\zeta_z \end{pmatrix},$$

where $J = \frac{\partial(\xi,\eta,\zeta)}{\partial(x,y,z)}$ is the Jacobian of the coordinate transformation between the curvilinear (ξ, η, ζ) and Cartesian (x, y, z) frames, and $\xi_x, \xi_y, \xi_z, \eta_x, \eta_y, \eta_z, \zeta_x, \zeta_y, \zeta_z$ are coordinate transformation metrics. ρ is the density. The three components of velocity are denoted by u, v, and w. E_t is the total energy given by

$$E_t = \frac{p}{\gamma - 1} + \frac{1}{2}\rho\left(u^2 + v^2 + w^2\right).$$

The contravariant velocity components U, V, W are defined as

$$U \equiv u\xi_x + v\xi_y + w\xi_z,$$

$$V \equiv u\eta_x + v\eta_y + w\eta_z,$$

$$W \equiv u\zeta_x + v\zeta_y + w\zeta_z.$$

The terms Q_x, Q_y, Q_z in the energy equation are defined as

$$Q_x = -q_x + u\tau_{xx} + v\tau_{xy} + w\tau_{xz},$$

$$Q_y = -q_y + u\tau_{xy} + v\tau_{yy} + w\tau_{yz},$$

$$Q_z = -q_z + u\tau_{xz} + v\tau_{yz} + w\tau_{zz};$$

The components of the viscous stress tensor and heat flux are denoted by τ_{xx}, τ_{yy}, τ_{zz}, τ_{xy}, τ_{xz}, τ_{yz}, and q_x, q_y, q_z, respectively.

In the dimensionless form, the reference values for length, density, velocities, temperature, pressure and time are L_r, ρ_r, U_r, T_r, $\rho_r U_r^2$, and L_r / U_r, respectively, where the subscript "*r*" denotes the reference quantities. The dimensionless parameters, including

the Mach number M, the Reynolds number Re, the Prandtl number Pr, and the ratio of specific heats γ, are defined as follows:

$$M = \frac{U_r}{\sqrt{\gamma R_g T}}, \quad Re = \frac{\rho_r U_r L_r}{\mu_r}, \quad Pr = \frac{C_p \mu_r}{k_r}, \quad \gamma = \frac{C_p}{C_v},$$

where R_g is the ideal gas constant, C_p and C_v are specific heats at constant pressure and constant volume, respectively. Viscosity is determined according to Sutherland's law in dimensionless form,

$$\mu = \frac{T^{3/2}(1+S)}{T+S}, \text{ and } S = \frac{110.3K}{T_\infty}.$$

The governing system is completed by the equation of state,

$$\gamma M^2 p = \rho T,$$

The components of the viscous stress tensor and the heat flux in their non-dimensional form are as follows:

$$\tau_{ij} = \frac{\mu}{Re}\left[\left(\frac{\partial u_i}{\partial x_j} + \frac{\partial u_j}{\partial x_i}\right) - \frac{2}{3}\delta_{ij}\frac{\partial u_k}{\partial x_k}\right]$$

$$q_i = -\frac{\mu}{(\gamma-1)M^2 Re\, Pr}\frac{\partial T}{\partial x_i}$$

2.2 *Numerical Algorithms and Parallel Computing*

The numerical simulation solves the three-dimensional compressible Navier-Stokes equations in generalized curvilinear coordinates using the implicit LU-SGS method [41]. A second-order fully implicit Euler backward scheme is used for the temporal discretization. The spatial derivatives appearing in the residual term are computed using the forth-order finite difference scheme in the interior of the domain. A sixth-order filter is applied at regular intervals in the simulation to suppress numerical oscillation.

The nonreflecting boundary conditions [18] are derived based on characteristic analysis. The modified Navier-Stokes equations are applied to the domain boundary and solved implicitly with the equations of interior points to ensure numerical stability.

Viscous terms are taken into account by including the viscous effect near the wall. The computation of the characteristic variables appeared in the modified Navier-Stokes equations depends on the direction of characteristic waves at the boundary. The corresponding characteristic variables of outgoing characteristic waves are computed from the interior nodes. The characteristic variables of incoming waves are determined by the boundary conditions. In the case of subsonic flow around airfoils, there are four incoming waves and only one outgoing wave at the inflow boundary. Thus, the freestream velocity and temperature are specified at this boundary, while the density is computed from interior points. Similarly, the nonreflecting boundary conditions also apply to the far-field, downstream, and no-slip adiabatic wall boundaries. More details of the mathematical model and numerical method can be found in [17, 18, 32].

The numerical simulation is performed using parallel computing with the Message Passing Interface (MPI) libraries. The computational domain is partitioned into n equal-sized sub-domains along the streamwise direction (ξ- direction) and each sub-domain is assigned to one processor. The implicit LU-SGS algorithm is implemented through a blockwise iteration within each processor and the solution data on the sub-domain interfaces are exchanged with neighboring processors at the end of iteration. The parallel computer code has been thoroughly tested on different platforms with the performance scaling almost linearly over a large number of processors.

2.3 *Immersed Boundary Method*

The immersed boundary method developed by Peskin [28] has been widely applied to numerical simulation of various flow problems. More recently, this method has been used for the simulation of three-dimensional flows by Goldstein *et al*.[13], Saiki and Biringen[29], Arthurs *et al*. [3], and Grigoriadis *et al*. [15]. The latest review is given by Mittal and Iaccarino [23]. The basic difference between the immersed boundary method and conventional approach lies in the way the solid boundaries are defined. Instead of using structured or unstructured boundary-fitting grids to define the geometrical configuration, the immersed-boundary method actually mimics the presence of solid bodies by means of suitably defined body forces. There are two different ways to impose

the body forces: the continuous forcing approach and the discrete forcing approach. In the first approach, which is suitable for solving flow problems with immersed elastic boundaries, the forcing term, usually formulated as a distribution function, is incorporated into the continuous momentum equation. In the second approach the forcing is introduced after the governing equations are discretized. The second approach is more attractive for flow problems involving solid boundary, which is tracked as a sharp interface. The introduction of forcing terms in the discrete forcing approach can be formulated in two methods: the indirect and direct boundary condition impositions. The indirect imposition still needs a smooth distribution function to distribute the forcing over several nodes near the interface. The implementation of the direct imposition is very straightforward, where the boundary conditions are directly imposed at immersed boundaries.

The focus of this work is to study the vortex generator induced large coherent vortical structures that convect downstream and introduce high momentum into boundary layer flow to eliminate or delay flow separation. The accuracy of numerical solution in resolving the vortex generator's self boundary layer has trivial effect on the convection and diffusion of streamwise vortical structures in the downstream [38]. Therefore, the immersed boundary method is an ideal technique for this case. In the present work, the discrete forcing approach with direct boundary condition imposition is used.

To validate the immersed boundary method, in particular the discrete forcing approach with direct boundary condition imposition, numerical experiments were performed on two test cases: the backward-facing step flow, and the flow past a circular cylinder. A detailed investigation on application of immersed boundary technique to these two examples can be found in [38] and [22]. In our test case of backward-facing step flow, the $22h \times 2h$ domain is partitioned by a non-uniform Cartesian grid with 220×65 points, where h is step height. Fig. 1 shows the mesh and the immersed boundary. The mesh is clustered near the surface of the step in both horizontal and vertical directions and near both top and bottom walls. The no-slip boundary condition is directly imposed on grid nodes located on the immersed boundary without interpolation and zero-velocity is specified at the interior nodes of the step. The Reynolds number based on the step height is 100 corresponding to a steady flow field. Fig. 2 shows the contours of streamwise

velocity. The negative value is shown by dashed contours. The reattachment length is about 3.7h, which is consistent with the experimental data [2] and numerical results with various immersed boundary methods [38].

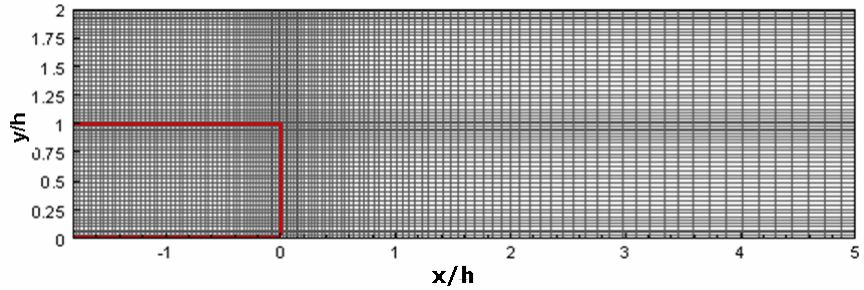

Fig. 1. Mesh near backward-facing step

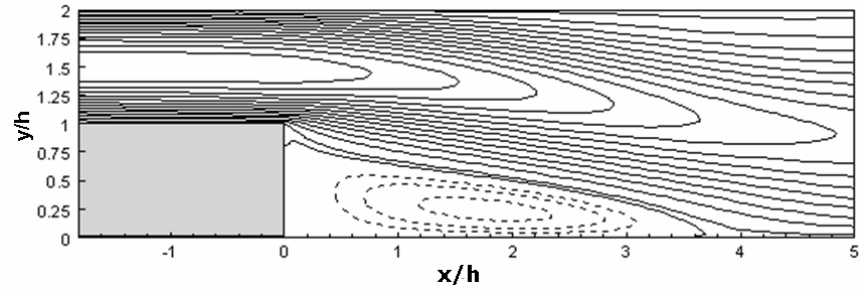

Fig. 2. Contours of streamwise velocity in backward-facing step flow

In the test case of flow past the circular cylinder, instead of using a Cartesian grid, the $56D \times 17D$ domain is partitioned by a curvilinear mesh with 364×259 grid points, where D is the diameter of the cylinder. The mesh is designed properly such that the immersed boundary (surface of the cylinder) conforms to the grid line and the mesh is clustered near the surface of the cylinder, as shown in Fig. 2.

The purpose of this is to avoid numerical interpolation in the immersed boundary method, thus the no-slip condition can be directly imposed on grid nodes that represent the surface of the cylinder. Zero-velocity is specified at the interior nodes of the cylinder. The Reynolds number based on freestream and diameter of the cylinder is 40 corresponding to the steady flow. A mesh with 364×259 grid points was used in the computation.

The contours of streamwise velocity are plotted in Fig. 4, where the negative contours are dashed. Fig. 5 shows the streamlines of the steady flow, where a, b, L, and θ represent the characteristic parameters used to describe the size and location of the

recirculation zone. Comparison of the present results with other computational [10] [22] and experimental [8] results at the same Reynolds number is given in Table 1. C_D is coefficient of drag. Our numerical results agree very well with others.

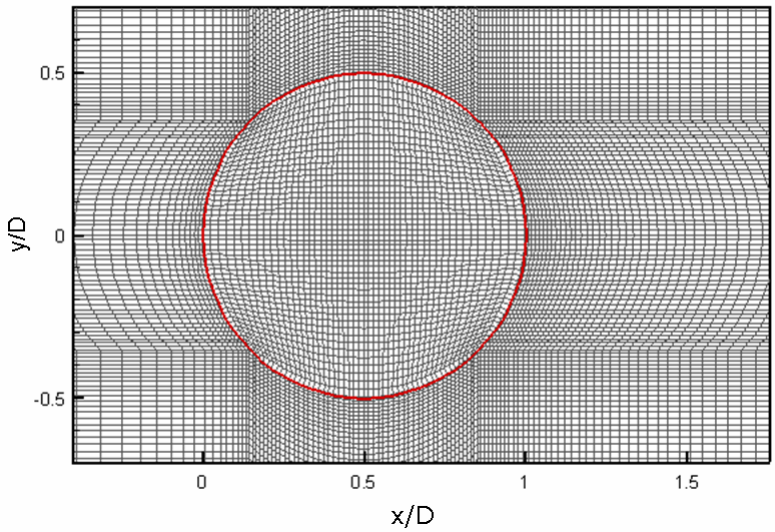

Fig. 3. Mesh around cylinder and the immersed boundary

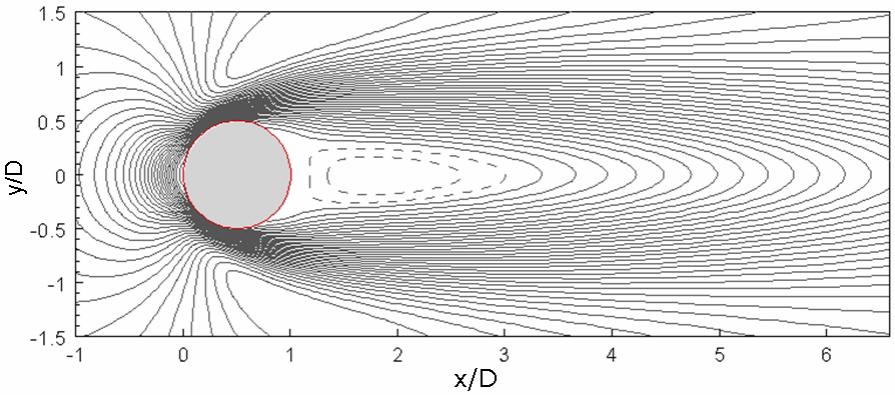

Fig. 4. Contours of streamwise velocity in steady flow past a circular cylinder

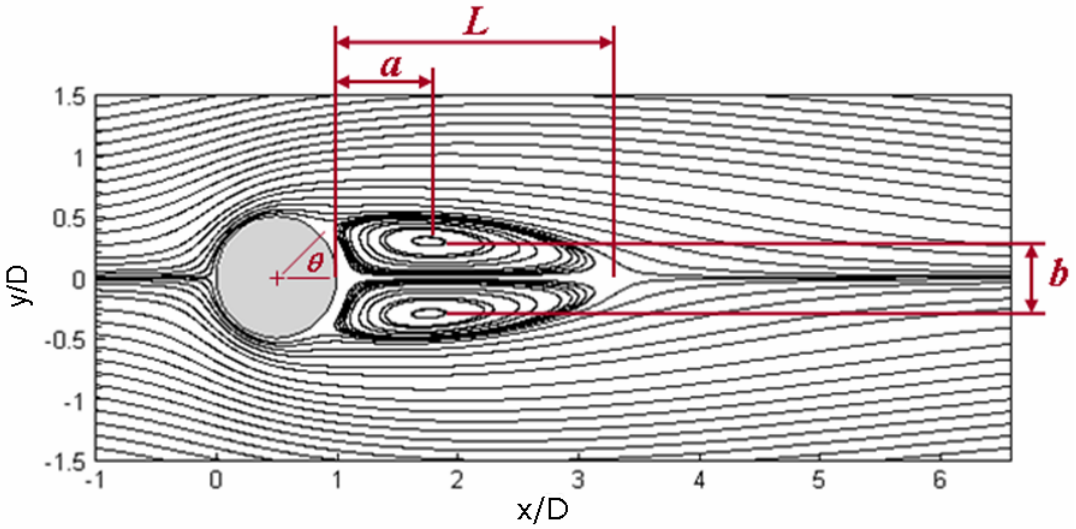

Fig. 5. Streamline of steady flow past a circular cylinder

Table 1. Comparison of present result with other computational/experimental results

	L	a	b	θ	C_D
Present result	2.25	0.759	0.589	53.9°	1.53
Linnick & Fasel [22]	2.28	0.72	0.60	53.6°	1.54
Coutanceau & Bouard [8]	2.13	0.76	0.59	53.8°	—
Fornberg [10]	2.24	—	—	55.6°	1.50

To further test the feasibility of simulating active vortex generator with the immersed boundary method. A numerical simulation of flow behind a pair of active vortex generators over a flat plate was performed [33] and satisfactory agreement was found when the numerical results were compared with experimental data [34]. Fig. 6 shows the contours of instantaneous streamwise velocity behind the vortex generators at their fully deployed and retracted positions during the first working duty cycle. In Fig. 6(a), the large scale streamwise vortical structures created by the vortex generators can be seen on the cross-sections (y-z plane). On x-y plane, the high-speed streaks appear at the downwash side of the streamwise vortices that bring high momentum fluid into the near wall region. In Fig. 6(b), the streamwise vortices disappear in the immediate downstream region after the vortex generators are fully retracted.

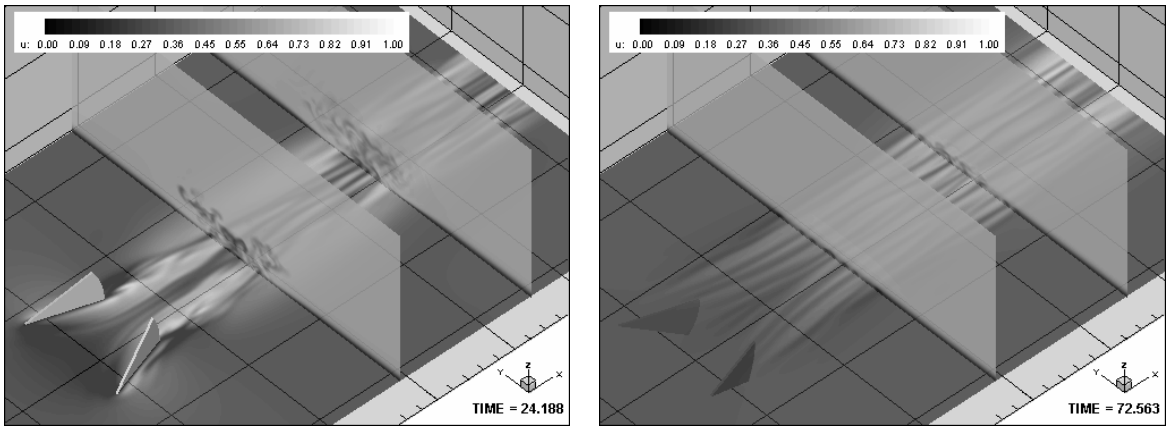

(a) fully deployed position (b) fully retracted postion

Fig. 6. Contours of instantaneous streamwise velocity behind a pair of active vortex generator over a flat plate

3. Problem Formulation

This study focuses on numerical simulation of flow separation and control over a NACA0012 airfoil at a 6° angle of attack. The characteristic scaling parameters for non-dimensionalization include the freestream velocity U_∞, the freestream pressure p_∞, the freestream temperature T_∞, and the chord length of the airfoil C. The characteristic time is defined as C/U_∞. Fig. 7(a) shows the layout of a pair of vortex generators on the surface of the airfoil, similar to the experiment of [34] except that the flat plate used in the experiment is replaced by the NACA0012 airfoil. The width of the airfoil is set to $0.1C$ in the simulation. The circular wing lip type vortex generator has a radius of $0.01675C$ and a thickness of $0.001C$. The vortex generator can rotate about its circular center (apex of the vortex generator) with a pitch angle ranging from 0° to 30.96° as shown in Fig. 7(b). The 0° pitch angle is corresponding to the fully retracted position and 30.96° to the fully deployed position. The maximum pitch of the vortex generator gives it a maximum height of $0.0086C$ normal to the airfoil surface. On the surface of the airfoil, the apex of the vortex generator is located at $x = 0.1C$, as shown in Fig. 7(c). The distance between the mid-chord points of the vortex generators is $0.02C$. The angle of yaw to the freestream flow is 18°. In the passive flow control simulation (Case 1), the vortex generators were deployed to their maximum height. In the active flow control simulation

(Case 2), the motion of two vortex generators was synchronized and controlled by a predefined duty cycle, which was set to a single sinusoidal function of time with a specified period in this study.

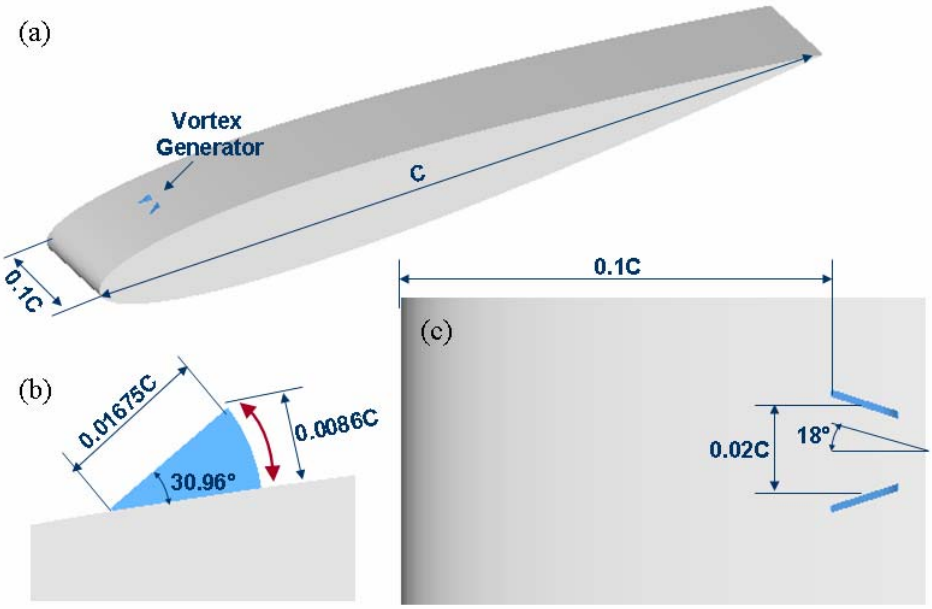

Fig. 7. NACA0012 airfoil and vortex generator
(a) perspective view; (b) side view; (c) top view

The body-fitted mesh is used to partition the domain around the NACA0012 airfoil as displayed in Fig. 8. In the ξ-ζ plane of the curvilinear coordinate system, the C-type mesh is generated numerically using an elliptic grid generation algorithm, where ξ, η, and ζ represent the streamwise, spanwise, and wall normal directions, respectively. The layout of mesh on the centerline plane and airfoil surface near the vortex generators is shown in Fig. 9. The upstream boundary of the computational domain is 3.5C from the leading edge of the airfoil. The outflow boundary is located at 5C downstream of the trailing edge. Because the nonreflecting boundary conditions are used, it is not necessary to use very large domain. The spanwise length of the domain is 0.1C. Since the numerical simulation is not designed to study the effect of an array of vortex generator pairs with redefined distance between each pair, a symmetry boundary condition is used on the boundary to avoid imposing a particular period in the spanwise direction.

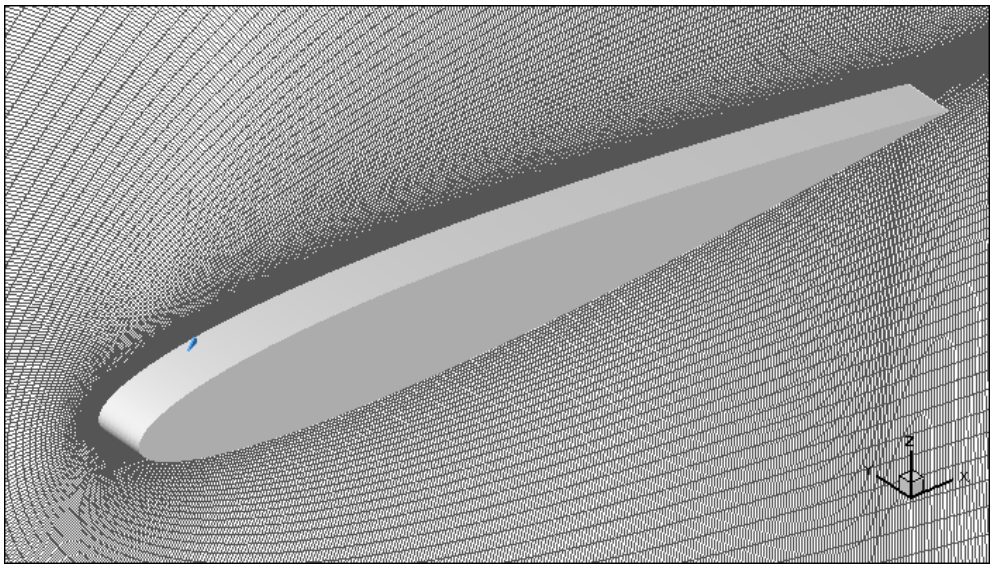

Fig. 8. Perspective view of the airfoil and mesh in ξ-ζ plane

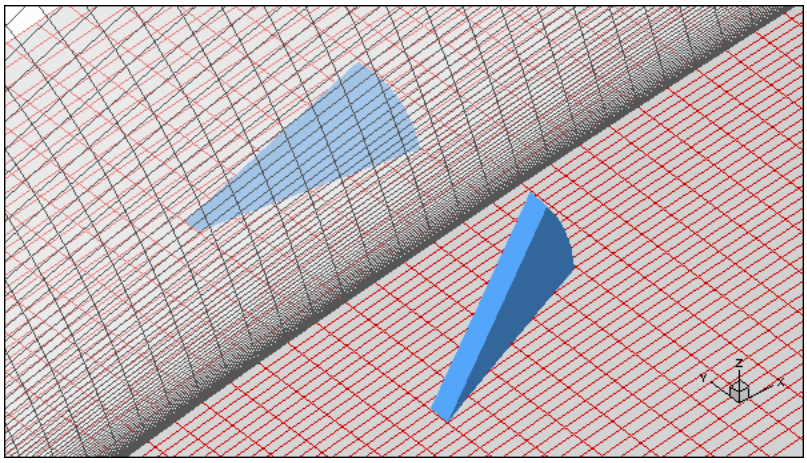

Fig. 9. Vortex generator and mesh on the upper surface of the airfoil and in ξ-ζ plane

The flow parameters used by the numerical simulation are summarized in Table 2. The Reynolds number based on the freestream velocity and the chord length is 10^5. The freestream Mach number is 0.2. The body-fitted mesh has $840 \times 90 \times 120$ grid points. Based on the wall unit of fully developed turbulent boundary layer flow, the grid size on the upper surface of the airfoil downstream of the vortex generator is $\Delta x^+ \approx 18$, $\Delta y^+ \approx 6$, and $\Delta z^+ \approx 0.75$. The time step size is $\Delta t = 1.09 \times 10^{-4}\, C / U_\infty$.

Table 2. Computational parameters

Angle of attack α	Reynolds number $Re = U_\infty C / \upsilon_\infty$	Mach number M	Grid nodes $N_\xi \times N_\eta \times N_\zeta$
6°	10^5	0.2	$840 \times 90 \times 120$

4. Numerical Results

The numerical simulations include three cases: uncontrolled flow separation (baseline case), flow separation control with a pair of passive vortex generators (Case 1), and flow separation control with a pair of active vortex generators (Case 2). The flow conditions and mesh used are exactly the same for all three cases. The numerical simulation results are summarized and compared in the following subsections.

4.1 *Baseline Case*

In the baseline case, the vortex generators are at their fully retracted position. The typical feature of the flow field can be seen from a side view of the isosurface of instantaneous spanwise vorticity with $\omega_y = 30$ as depicted in Fig. 10. The separation of free shear layer from the airfoil surface, vortex shedding from the separated shear layer, reattachment of the shear layer, and breakdown to turbulence in the boundary layer can be seen clearly in the figure.

Fig. 10. Isosurface of instantaneous spanwise vorticity ($\omega_y = 30$)

Fig. 11 shows the time- and spanwise-averaged velocity vectors at every third streamwise grid location and the contours of streamwise velocity. The time-average was performed over a time period of $15 C / U_\infty$. The contours of the reversed flow with negative streamwise velocity are plotted in a dark color. The mean flow field in Fig. 11

indicates that the separation starts at $x = 0.06C$ near the leading edge of the airfoil. The separated flow reattaches near $x = 0.285C$. The average length of the separation bubble is about $0.225C$. The streamlines of the mean flow field are plotted in Fig. 12. Besides the location of the mean separation and reattachment points, Fig. 12 also shows the center of the mean recirculation bubble in the separation zone. The characteristic length of the separation region L_{sep}, defined as the distance between the separation point and the center of the mean recirculation bubble [24], is about $0.18C$ in the baseline case.

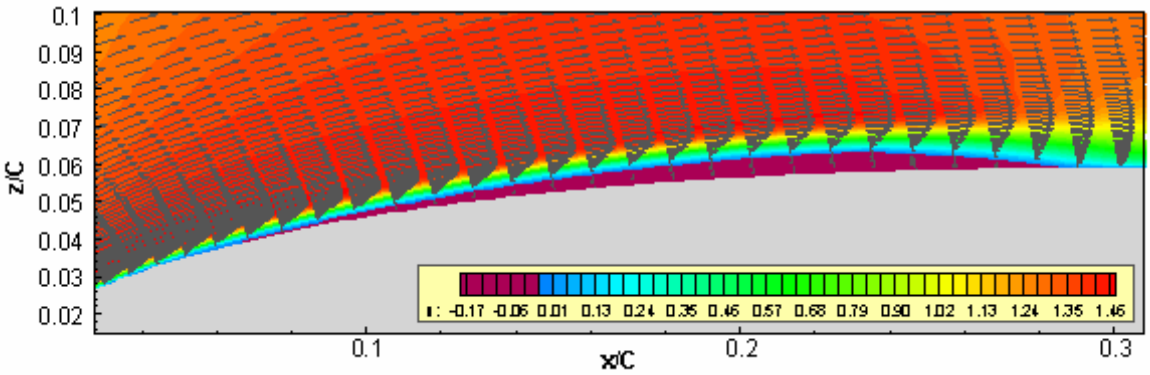

Fig. 11. Time and spanwise averaged velocity vectors and contours of baseline case (Every third streamwise grid location is shown)

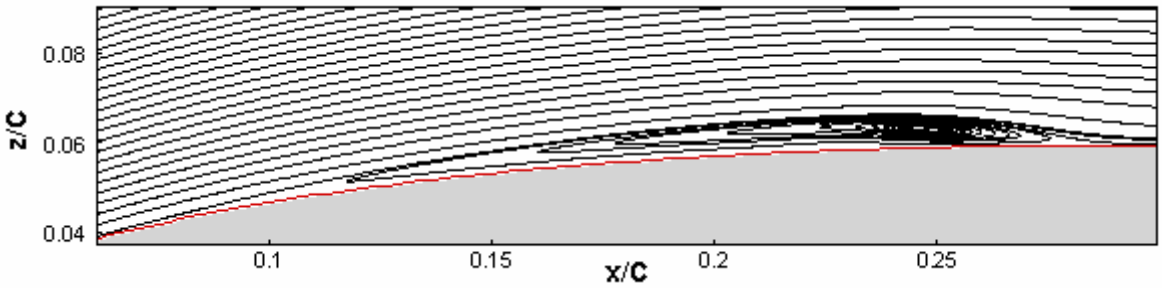

Fig. 12. Time- and spanwise-averaged streamlines of baseline case.

Fig. 13 shows the mean pressure coefficient C_p of the airfoil calculated from the time- and spanwise-averaged result. Near the leading edge, the strong adverse pressure gradient on the upper surface causes the separation of the boundary layer near the leading edge. The suction plateau that follows the suction peak corresponds to the separation bubble. The skin friction coefficient C_f of the mean flow on the upper surface of the

airfoil is shown in Fig. 14. The negative value of C_f between $x = 0.06C$ and $x = 0.285C$, indicates the near-wall reversed flow in the separation bubble. Both Fig. 13 and Fig. 14 confirm the observation in Fig. 11 and Fig. 12 in terms of the location and length of the separation bubble. The abrupt recovery of C_f from its negative peak to a positive peak between $x = 0.25C$ and $x = 0.35C$ corresponds to transition and reattachment of the separated flow.

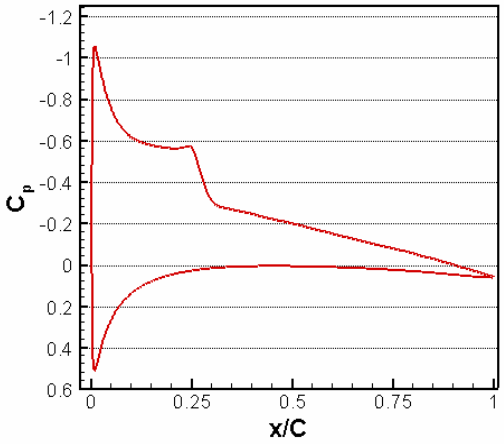

Fig. 13. Mean pressure coefficient of baseline case

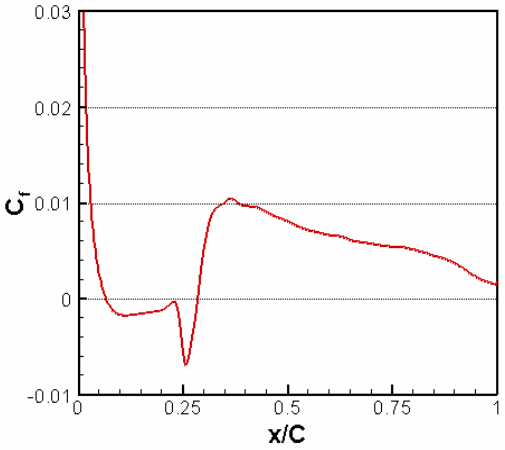

Fig. 14. Mean skin friction coefficient of baseline case

The chord-wise distribution of peak turbulence kinetic energy k is displayed in Fig. 15. The 'peak' means the maximum k at each streamwise location. The abrupt increase of k at $x \approx 0.24C$ indicates the starting point of transition to turbulence, which is also shown by the sharp increase of C_f displayed in Fig. 14. It is clear that transition occurs before the separated flows reattaches, because the mean reattachment point is at $x = 0.285C$ while transition starts at $x \approx 0.24C$.

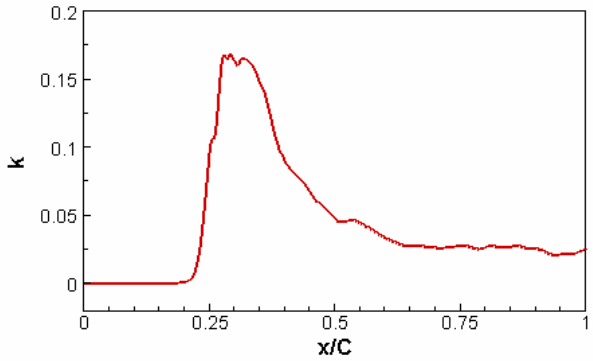

Fig. 15. Chord-wise distribution of peak turbulence kinetic energy of baseline case.

The three-dimensional isosurfaces of the instantaneous streamwise, spanwise, and wall-normal components of vorticity over the upper surface of the airfoil are shown in Fig. 16. The three-dimensional vortical structures appear after the transition and reattachment as shown in Fig. 16(a), (b) and (c), where the contours of streamwise vorticity ω_x, spanwise vorticity ω_y, and wall-normal vorticity ω_z are displayed. The separated shear layer can be seen from the isosurface of the spanwise vorticity in Fig. 16(b). Near the leading edge of the airfoil, a two-dimensional shear layer is detached from the surface and no three-dimensional streamwise vortical structure can be seen near the separation point. Therefore, the separated shear layer is initially a two-dimensional laminar flow. Then slight distortions become visible on the isosurface of the spanwise vorticity and the three-dimensional fluctuations start to grow rapidly and eventually lead to the shedding of vortices indicating that the separated shear layer undergoes transition, which is followed by reattachment of the separated shear layer, and breakdown of small-scale three-dimensional structures in the immediate downstream region of reattachment. Fig. 16(a) also indicates that the downstream region of the reattachment point between $x = 0.25C$ and $x = 0.5C$ is the most active area that contains more vortical structures.

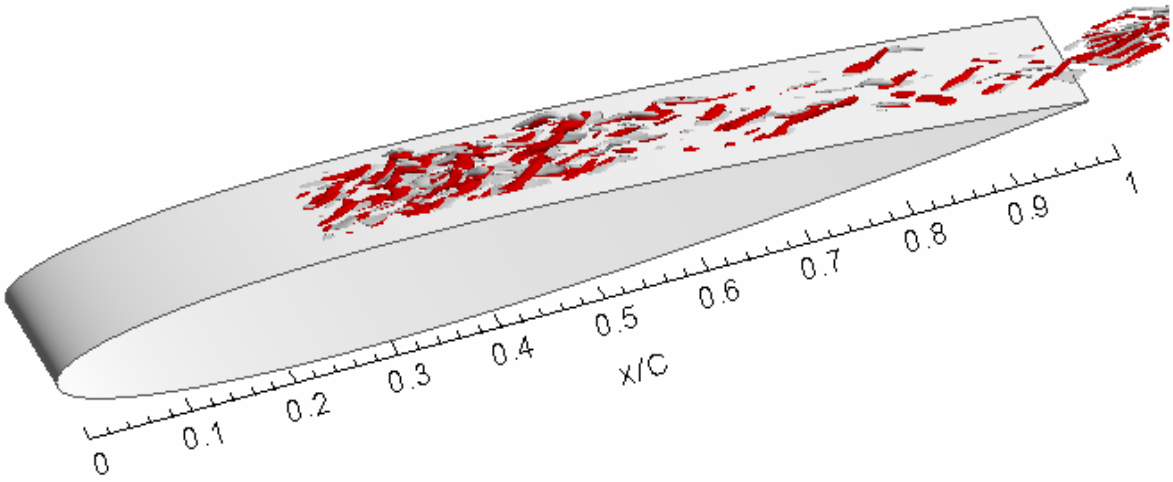

(a) streamwise vorticity
(dark color: $\omega_x = 100$; light color: $\omega_x = -100$)

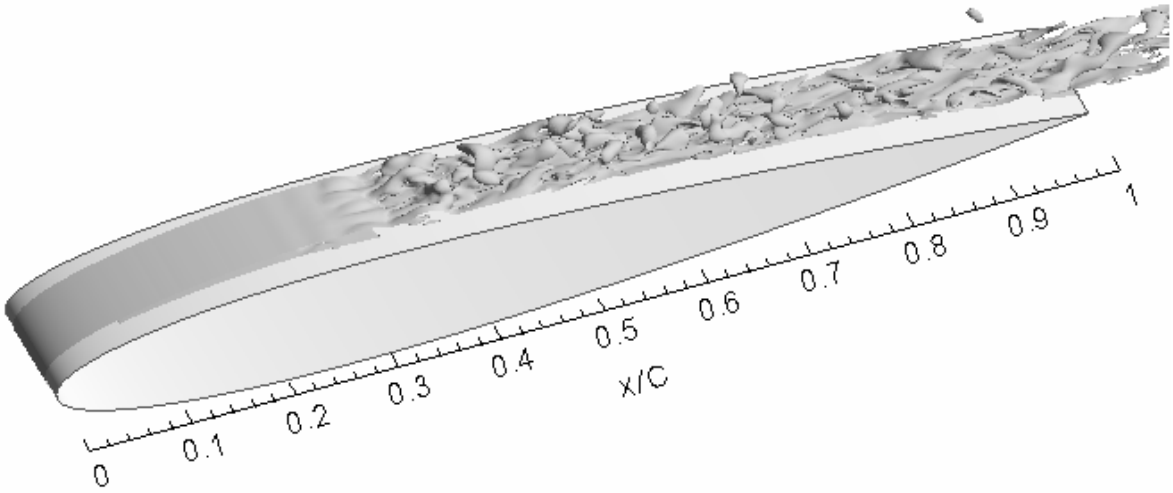

(b) spwanwise vorticity
(color: $\omega_y = 30$)

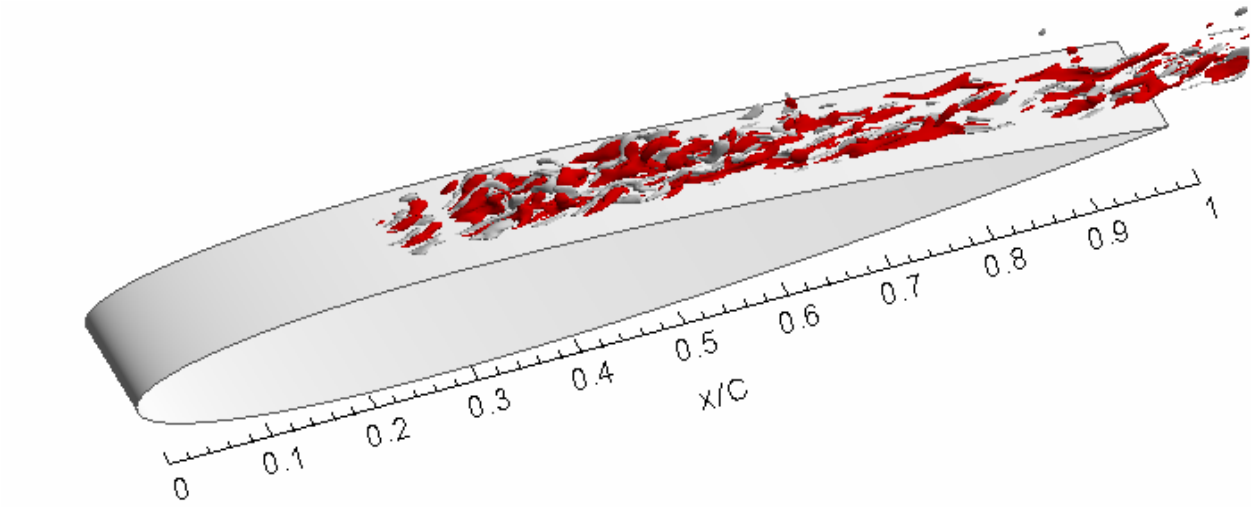

(c) wall-normal vorticity
(dark color: $\omega_z = 50$; light color: $\omega_z = -50$)

Fig. 16. Three-dimensional isosurface of components of instantaneous vorticity of baseline case

In order to identify the natural frequency of flow separation in the baseline case, spectrum of pressure fluctuations was computed from simulation data at several streamwise stations. Fig. 17 shows the spectra of pressure fluctuations at $x = 0.163C$ and $x = 0.217C$ on the centerline plane and near the upper surface of the airfoil. Fig. 17(a) has a small peak at $f \approx 15\, U_\infty / C$ which becomes the dominant spectrum at the downstream location of $x = 0.217C$ as shown in Fig. 17(b). The peak spectrum at $f \approx 15\, U_\infty / C$ reflects the natural characteristic frequency of the flow separation region (f_{sep}), a frequency at which vortices are shedding from the separated shear layer [24]. A careful examination of the animated flow structures from simulation data also confirms this conclusion. Apparently f_{sep} is the dominant frequency in the baseline case. Fig. 17(b) also indicates that f_{sep} is not an isolated spectrum peak and a broad and strong spectrum of other frequencies appears as a wave packet centered at f_{sep}. The similar wave packets have also been observed in the experiments of Yarusevych et al. [40].

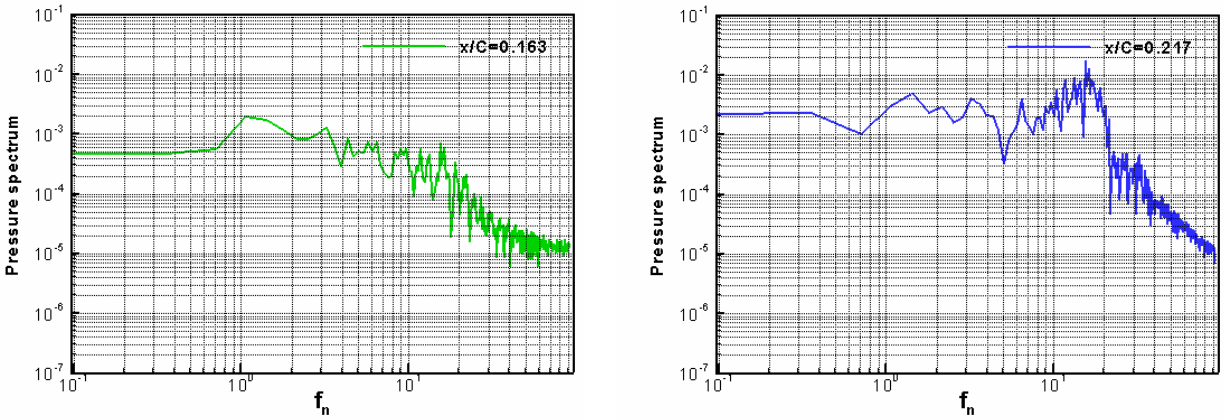

(a) $x = 0.163C$ (b) $x = 0.217C$

Fig. 17. Spectra of pressure fluctuations of baseline case

4.2 *Case 1 – Flow Separation Control with Passive Vortex Generators*

In this case, a pair of static vortex generators is used for passive flow separation control. The details of the layout of vortex generators were presented in Section 3. It is worth to note that the apex of the vortex generator is located at $x = 0.1C$, which is very close to the location of the mean separation point at $x = 0.06C$ in the uncontrolled baseline case. The vortex generators are fully deployed to their maximum height which is about two times the local boundary layer thickness. It should be pointed out that geometric parameters of the vortex generators, such as size, pitch and yaw angles, distance between vanes, and streamwise location, are not to be optimized in this study.

Fig. 18 shows the time- and spanwise-averaged velocity vector and contours of streamwise velocity. The time-average was performed over a time period of $25C/U_\infty$. Fig. 19 plots the streamlines of the time- and spanwise-averaged flow field. Compared with the uncontrolled baseline case shown in Fig. 11, the strong recirculation and the size of separation bubble has been substantially reduced. Two small separation bubbles can be identified in the mean flow displayed in Fig. 18. The first bubble starts at the natural separation point near $x = 0.06C$ and is forced to reattach at about $x = 0.11C$. Then the mean flow remains attached behind the vortex generators over a significant extent of the airfoil until $x = 0.21C$, the starting point of a second separation which reattaches near $x =$

0.25C forming a small separation bubble with a length of about 0.04C. The numerical results indicate that the passive vortex generator leads to a more than 80% reduction in the length of separation bubble compared with the baseline case.

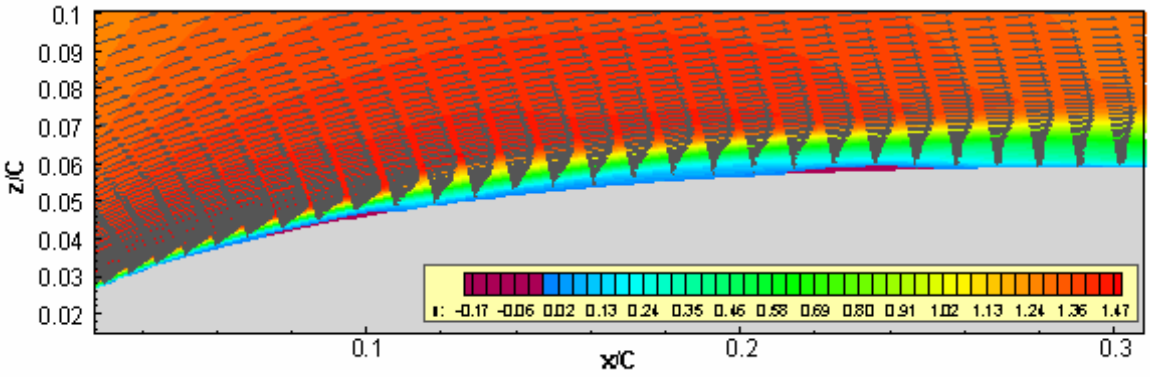

Fig. 18. Time and spanwise averaged velocity vectors and contours of Case 1 (Every third streamwise grid location is shown)

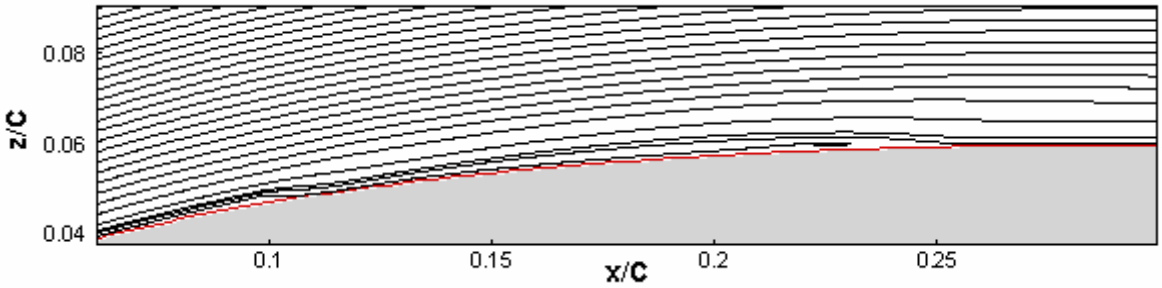

Fig. 19. Time- and spanwise-averaged streamlines of Case 1.

The mean pressure coefficient C_p is shown in Fig. 20 in comparison with that of the baseline case. The suction plateau has been significantly reduced. The C_p curves from both cases almost coincide with each other downstream of reattachment, indicating that the vortex generator has minor effect on mean pressure distribution downstream of the reattachment ($x > 0.4C$). The comparison between the friction coefficient C_f of the two cases is displayed in Fig. 21. The C_f of Case 1 remains positive except for the two segments corresponding to the small separation bubbles that appear in Fig. 18 and Fig. 19. There is a sharp increase in C_f immediately downstream of the vortex generator indicating that the friction is increased due to the high momentum fluid brought by the vortex generator into the near wall region.

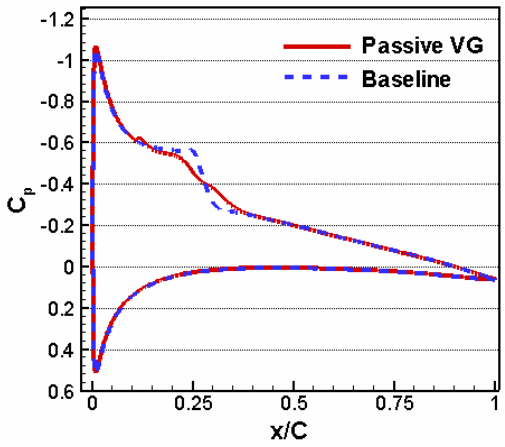

Fig. 20. Mean pressure coefficient of Case 1 in comparison with baseline case

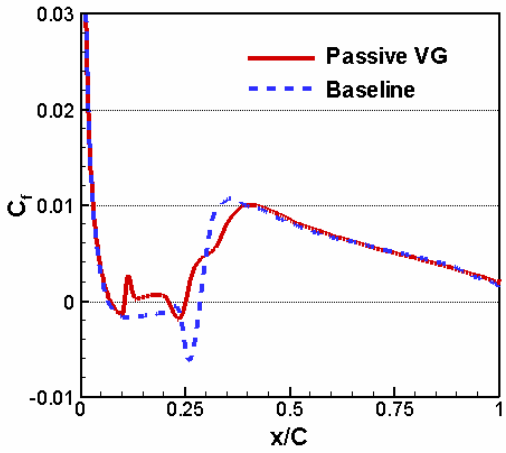

Fig. 21. Mean skin friction coefficient of Case 1 in comparison with baseline case

Fig. 22 shows the chord-wise distribution of the peak turbulence kinetic energy k of Case 1 in comparison with that of the baseline case. In Case 1, k increases sharply at $x \approx 0.24C$, about the same location in the baseline case. It should be noted that the passive vortex generators only reduce the size of the natural separation bubble and there are still two small separation bubbles remaining in the time and spanwise averaged result as shown in Fig. 18. In this case, the high momentum transferred from the freestream by vortices created by the passive vortex generators reattaches the separated laminar flow forming the first bubble between $x = 0.06C$ and $x = 0.11C$. But the reattached laminar flow is not able to resist the adverse pressure gradient downstream and it separates again from the airfoil surface near $x = 0.21C$. The separated shear layer undergoes transition which leads to reattachment at $x = 0.25C$ forming the second bubble as shown in Fig. 18. In this case, as displayed in Fig. 22, transition in the second separated shear layer occurs at approximately the same location as in the baseline case. It is possible that the vortices created by the passive vortex generators bring more energy to the transition process such that the maximum peak k is almost three times higher than that of the baseline case.

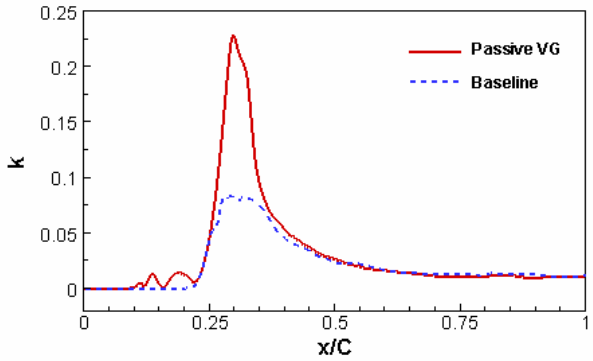

Fig. 22. Chord-wise distribution of peak turbulence kinetic energy of Case 1 in comparison with baseline case.

Fig. 23 shows the three-dimensional isosurfaces of the instantaneous streamwise, spanwise, and wall-normal vorticity over the upper surface of the airfoil. The passive vortex generators at $x = 0.1C$ produce a pair of counter-rotating streamwise vortices in the immediate downstream region, see Fig. 23(a). These vortices are the only three-dimensional structures upstream of $x = 0.2C$. They bring high momentum fluid into the near-wall region and reattach the separated flow as shown in Fig. 23(b). The reattached flow separates again at about $x = 0.2C$ which is very close to the mean separation point The animated flow field also shows a steady location of the second separation point. The animation also shows that the instantaneous reattachment point wanders between $x = 0.25C$ and $x = 0.3C$. At the instant shown by Fig. 23, the reattachment occurs at about $x = 0.3C$. Fig. 23 also shows the most active vortical structures between $x = 0.3C$ and $x = 0.5C$ which is consistent with the distribution of peak turbulence kinetic energy in Fig. 22.

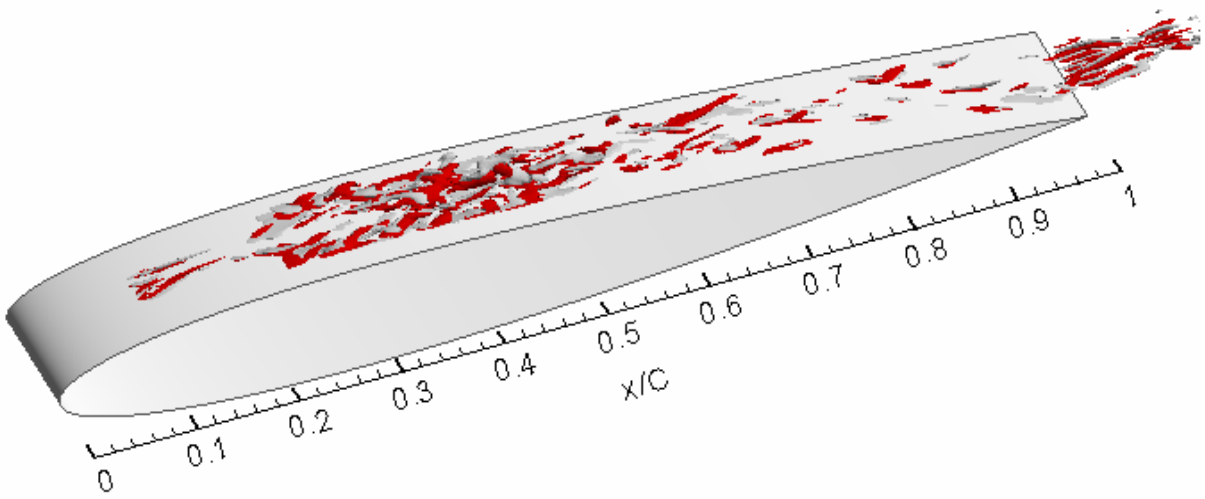

(a) streamwise vorticity
(dark color: $\omega_x = 100$; light color: $\omega_x = -100$)

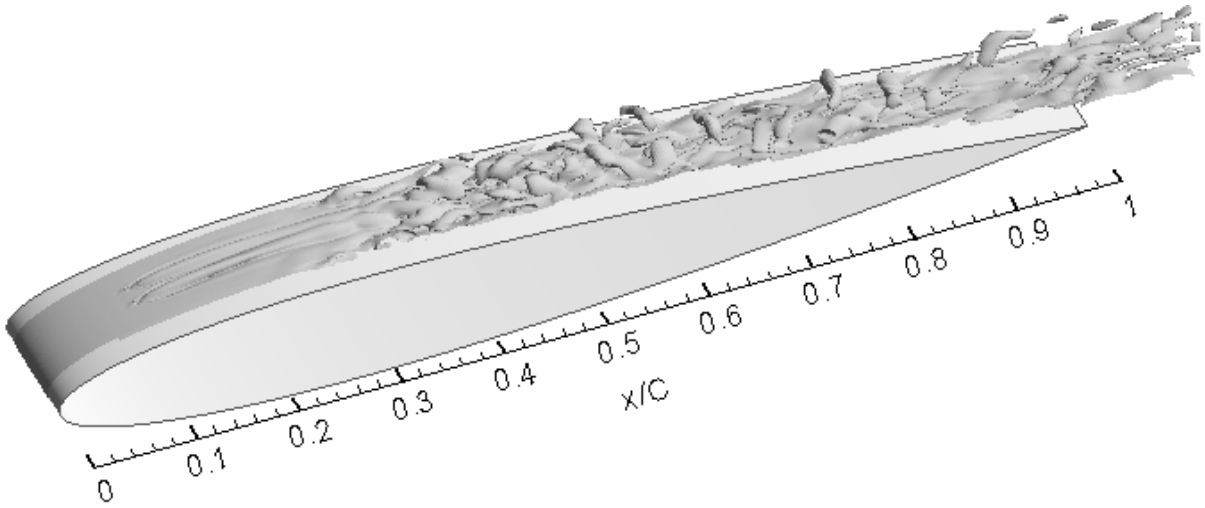

(b) spwanwise vorticity
($\omega_y = 30$)

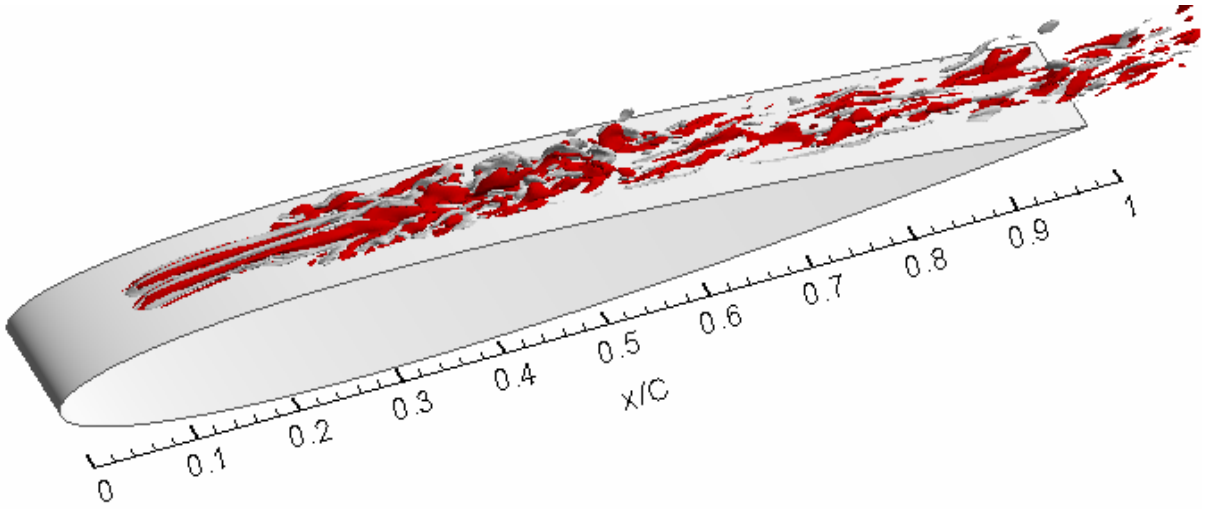

(c) wall-normal vorticity
(dark color: $\omega_z = 50$; light color: $\omega_z = -50$)

Fig. 23. Three-dimensional isosurface of components of instantaneous vorticity of Case 1.

The time- and spanwise-averaged results have shown that the second separation starts at $x = 0.21C$ and transition occurs at $x = 0.24C$. The spectrum of pressure fluctuations was computed from simulation data to identify the frequency of flow separation. .The spectra of pressure fluctuations at $x = 0.163C$ and $x = 0.217C$ are displayed in Fig. 24. Compared with in Fig. 17(a), the peak spectrum $f \approx 15\, U_\infty / C$ that appears in the uncontrolled baseline case is not visible in Fig. 24(a), as the separated shear layer reattaches due to streamwise vortices created by the passive vortex generators. However, at $x = 0.217C$ within the second separation bubble, a spectrum peak is found at $f \approx 15\, U_\infty / C$ as shown in Fig. 24(b). This frequency equals f_{sep} – the natural characteristic frequency of flow separation in the baseline case. It is also confirmed by the animated flow visualization of the simulation data that vortices are shedding from the second separated shear layer at a frequency of f_{sep}, indicating that mechanism of flow transition in Case 1 is similar to that of baseline case. Despite the similarity, the spectra of these two cases have obvious difference that Case 1 has a standalone and smaller peak at f_{sep} and the baseline case has a stronger wave packet centered at f_{sep}, see Fig. 17(b) and Fig. 24(b). A possible explanation is as follows: In the baseline case, the initial separation occurs at $x = 0.06C$. The instability in the separated shear layer develops and evolves into an amplified disturbance involving more frequencies such that the spectrum

at $x = 0.217C$ shows a wave packet with a higher peak centered at f_{sep}. In Case 1, the second separation bubble starts at $x = 0.21C$, and it is not surprise that its spectrum at $x = 0.217C$ has an isolated peak at f_{sep}.

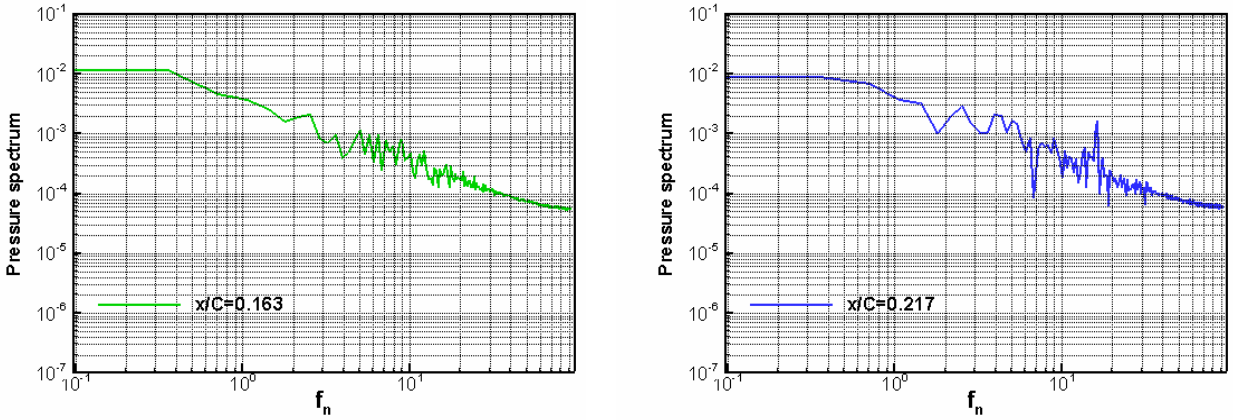

(a) $x = 0.163C$ (b) $x = 0.217C$

Fig. 24. Spectra of pressure fluctuations of Case 1

4.3 *Case 2 – Flow Separation Control with Active Vortex Generators*

In controlled case 2, a pair of oscillating vortex generators was used for active flow separation control. The vortex generator layout can be found in Section 3. The location of the vortex generators is the same as in controlled case 2. The motion of two vortex generators was synchronized and controlled by a sinusoidal duty cycle with a frequency of $f_e = 15\,U_\infty / C$ that equals the natural frequency of the separation region in the baseline case. It has been reported that the range of effective frequency of excitation includes bands of naturally amplified frequencies centered at f_{sep} and the normalized frequency of excitation should be $F^+ = f_e / f_{sep} = O(1)$ [24, 39]. Given the length of natural separation bubble $X_B = 0.225C$ in the uncontrolled baseline case, there is an alternative way to normalize f_e as $f_e X_B / U_\infty = 3.4$, which is consistent with the general range of $0.3 \le f_e X_B / U_\infty \le 4$ obtained by experiments [14].

A time- and spanwise- average was performed over the simulation data with a time period of $30C/U_\infty$. Fig. 25 shows the averaged velocity vector and contours of streamwise velocity. The separation is not visible in the mean flow field as it is also confirmed by plotting the mean streamlines in Fig. 26. Compared with Case 1, the active vortex generator with an excitation frequency equaling the natural frequency of separation is more effective than the passive vortex generator in terms of controlling the size of separation bubble.

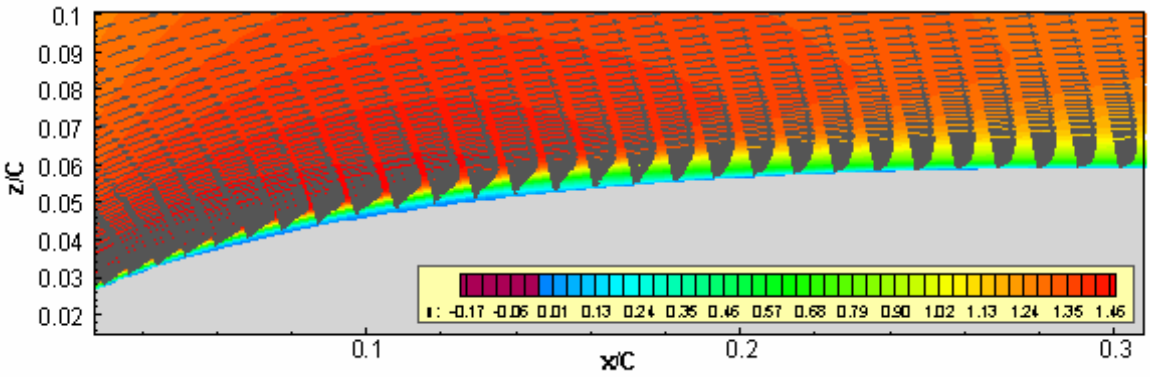

Fig. 25. Time and spanwise averaged velocity vectors and contours in Case 2 (Every third streamwise grid location is shown)

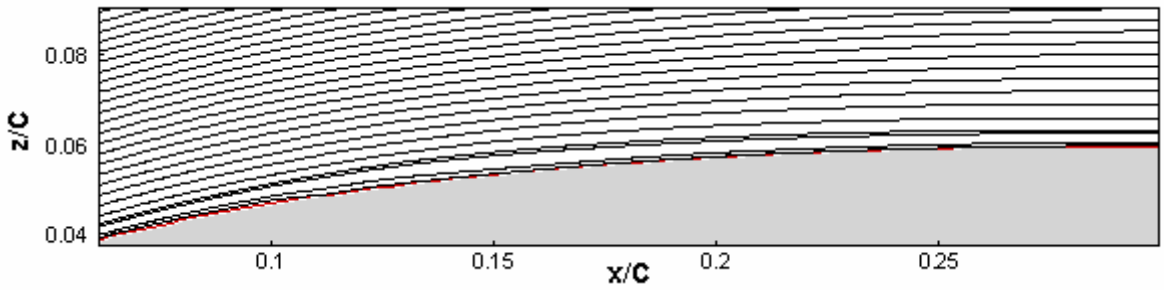

Fig. 26. Time- and spanwise-averaged streamlines of Case 2.

The comparison of mean pressure coefficient C_p of controlled case 2 with the baseline case and controlled case 1 is shown in Fig. 27. Case 2 produces a more desirable C_p curve, because the suction plateau is removed. The C_p curves from all three cases almost coincide with each other downstream for $x > 0.4C$, indicating that the active vortex generator has minor effect on the average pressure distribution over the aft portion

of the airfoil at this angle of attack. The friction coefficient C_f of all the three cases is shown in Fig. 28. In Case 2, there is a sharp increase in C_f immediately downstream of the active vortex generators, which brings in extra kinetic energy to the flow field and leads to an early transition.

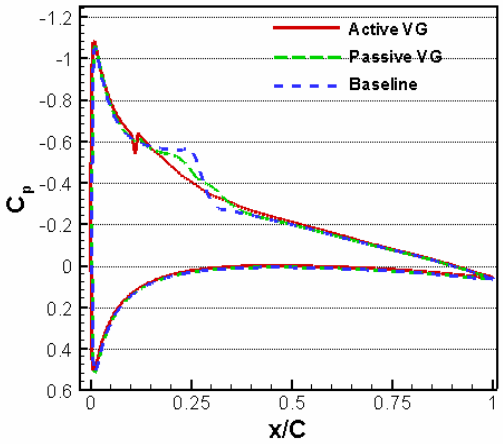

Fig. 27. Mean pressure coefficient of Case 2 in comparison with baseline and Case 1

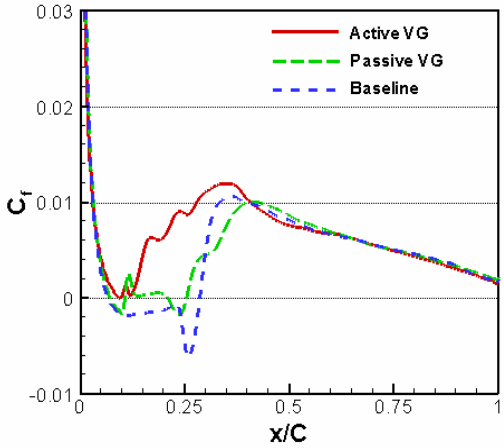

Fig. 28. Mean skin friction coefficient of Case 2 in comparison with baseline and Case 1

A comparison of the chord-wise distribution of peak turbulence kinetic energy k of all three cases is given in Fig. 29. It is obvious that the active vortex generators located at $x = 0.1C$ have triggered immediate transition downstream as there is an abrupt rise in k starting at $x = 0.1C$. The mechanism of transition and separation control in this case is probably different from that of the baseline case and Case 1, where the transition occurs in the separated shear layer due to amplification of the Kelvin-Helmholtz type instability. In Case 1, the reduction in bubble size is caused by the streamwise vortices created by the passive vortex generators. The momentum transferred by the vortices enforces the separated flow to reattach. But in further downstream region, the reattached flow fails to resist the pressure rise and separates again, followed by the transition in separated shear layer and reattachment. In Case 2, the early transition process triggered by the active vortex generators must play an important role in eliminating the separation bubble. Otherwise the reattached flow would separated again as it happens in Case 1, because the streamwise vortices created by the periodic motion of the active vortex generators do not sustain after the vanes are fully retracted during a duty cycle. Also compared to the

passive vortex generators that stay at their maximum height all the time, the active vortex generators have less capability of bringing high momentum into the lower boundary layer. On the other hand, transition increases entrainment and enables momentum transfer from mainstream to boundary layer. Therefore, it must be the early transition triggered by the active vortex generators that eliminates the separation bubble.

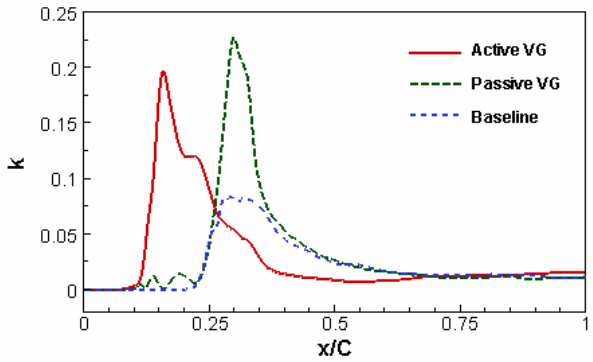

Fig. 29. Chord-wise distribution of peak turbulence kinetic energy of Case 2 in comparison with baseline case.

Fig. 30 shows the three-dimensional isosurfaces of the instantaneous streamwise, spanwise, and wall-normal vorticity over the upper surface of the airfoil. Transition occurs in the immediate downstream region of the active vortex generators located at x = 0.1C. The periodically created streamwise vortices travel downstream and form a train of vortex tubes that are still visible up to x = 0.5C as shown in Fig. 30(a). As one looks carefully at the further downstream region with x > 0.5~0.6C, the instantaneous flow fields of all three cases are qualitatively similar to each other, see Fig. 16, Fig. 23, and Fig. 30. It appears also in the averaged results that the C_p and C_f curves of all three cases overlap in the downstream region, as shown in Fig. 27 and Fig. 28.

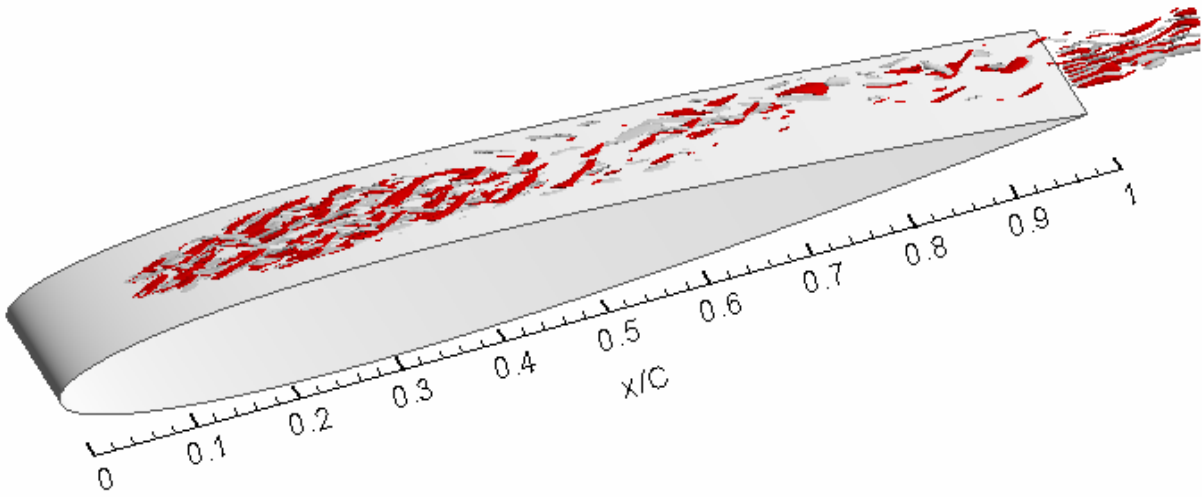

(a) streamwise vorticity
(dark color: $\omega_x = 100$; light color: $\omega_x = -100$)

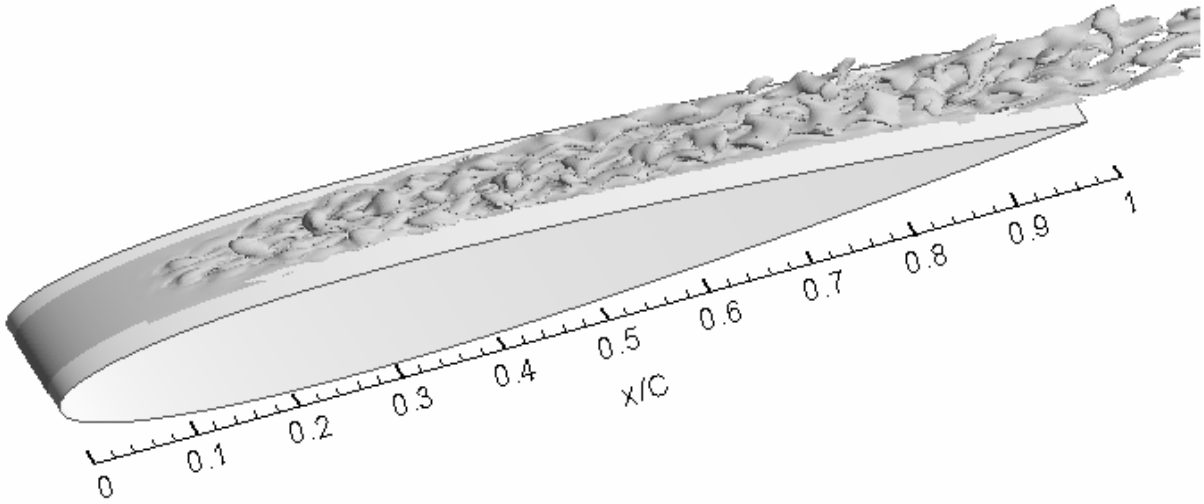

(b) spwanwise vorticity
($\omega_y = 30$)

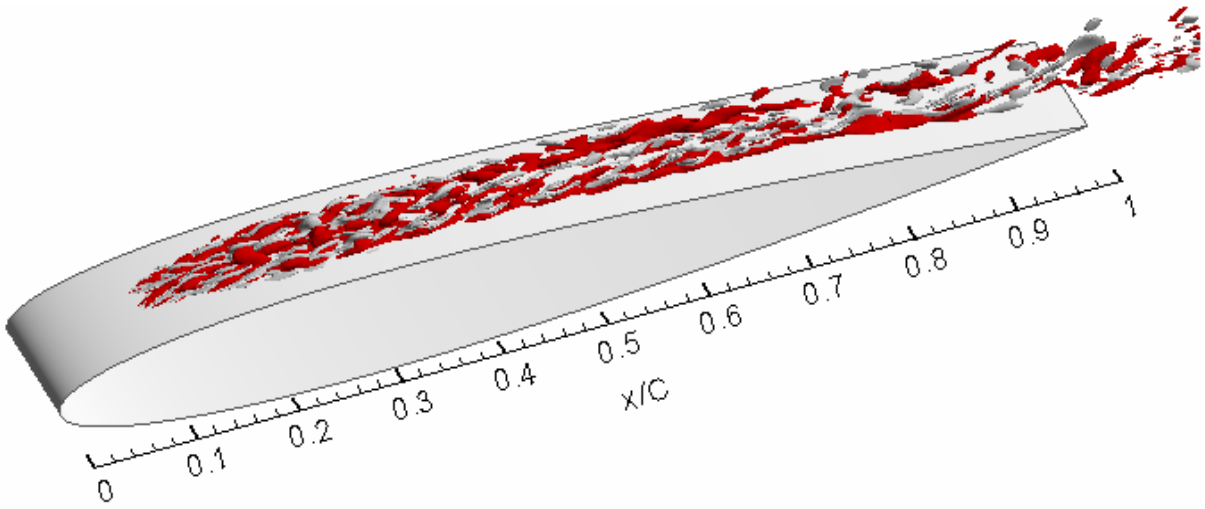

(c) wall-normal vorticity
(dark color: $\omega_z = 50$; light color: $\omega_z = -50$)

Fig. 30. Three-dimensional isosurface of components of instantaneous vorticity of Case 2.

In Case 2, the excitation frequency is $f_e = 15\, U_\infty / C$. The spectra of pressure fluctuations at x = 0.163C, x = 0.217C, x = 0.312C, and x = 0.577C on the centerline plane near the upper surface of the airfoil are displayed in Fig. 31. The first peak from the left corresponds to f_e. The spectrum peaks corresponding to its harmonics at $30\, U_\infty / C$, $45\, U_\infty / C$, $60\, U_\infty / C$, and $70\, U_\infty / C$ are also seen in Fig. 31(a), (b), and (c). The harmonic peaks of f_e disappear in the spectrum at x = 0.577C as shown in Fig. 31(d). Fig. 31 indicates that the flow between the vortex generators and mid-chord is dominated by f_e and its harmonics.

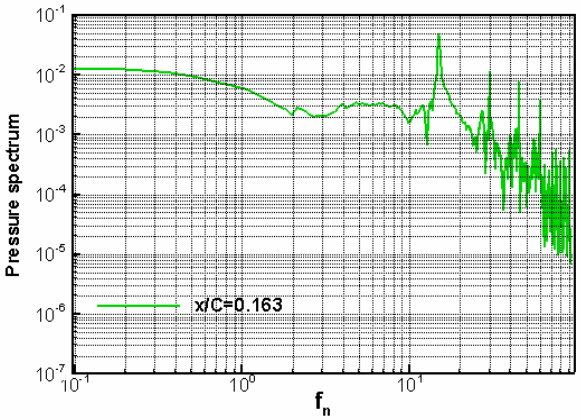

(a) $x = 0.163C$

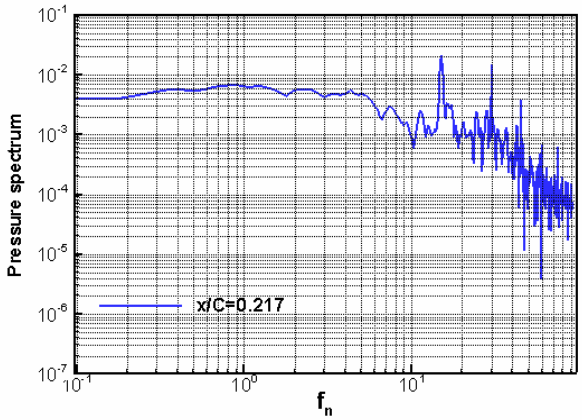

(b) $x = 0.217C$

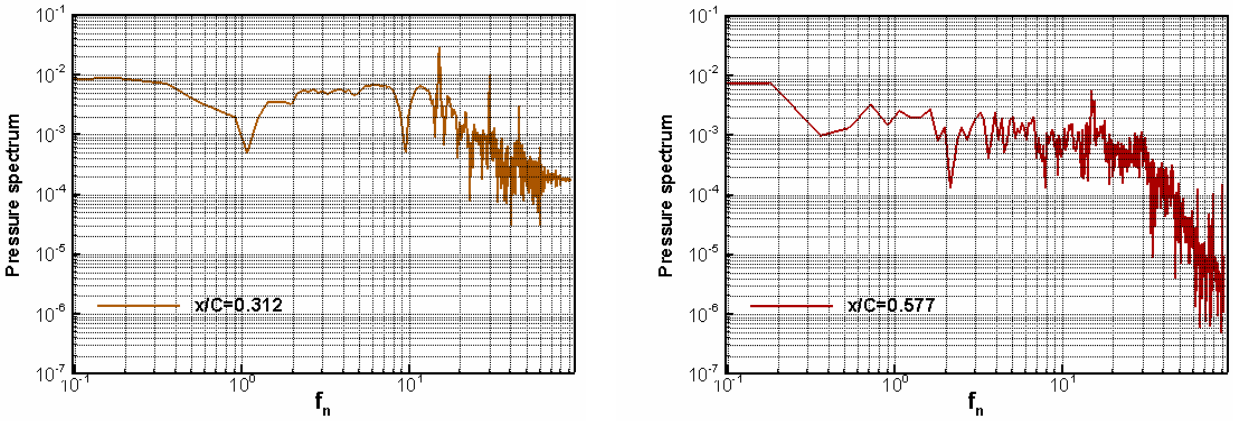

I $x = 0.312C$ (d) $x = 0.577C$

Fig. 31. Spectra of pressure fluctuations of Case 2

5. Concluding Remarks

We have studied the flow separation control with vortex generators using an approach that combines the body-fitted mesh for the airfoil in a curvilinear coordinate system and the immersed boundary method for the vortex generator in the context of direct numerical simulation. Our study includes the following three cases: 1) uncontrolled flow separation (baseline case), 2) flow separation control with passive vortex generators (Case 1), and 3) flow separation control with active vortex generated (Case 2) over a NACA0102 airfoil at a 6° angle of attack. In the uncontrolled baseline case, the naturally separated flow is dominated by $f_{sep} \approx 15\, U_\infty / C$, which represents the frequency of vortex shedding from the separated shear layer. In Case 1, the time- and span-wise averaged results have shown that the passive vortex generators are able to reattach the separated flow in the immediate downstream region over an extent of $0.1C$. However, the reattached flow separates again and the separated shear layer undergoes transition and reattachment forming the second separation bubble. Thus, the passive vortex generators reduce the size of the separation zone by more than 80%. The simulation of Case 2 has shown that active vortex generators are more effective than the passive ones because the separation is not visible in the time- and span-wise averaged mean flow. At the small angle of attack simulated in this study, flow separation control does not produce significant gain in lift or reduction in drag, but it does provide a first step leading toward a more thorough understanding of

flow control with active vortex generators. The future work should emphasis on numerical simulations of flow separation and control over airfoils at larger angles of attack (e.g. ≥ 15°).

Acknowledgments

The presented research work was supported in part by the Lockheed Martin Aeronautic Company.

References

1. Alam, M. and Sandham, N.D. 2000 Direct numerical simulation of 'short' laminar separation bubbles with turbulent reattachment. *J. Fluid Mech.* 410, 1-28.
2. Armaly, B.F., Durst, F., Pereira, J.C.F., Schonung, B. 1983 Experimental and theoretical investigation of backward-facing step flow. *J. Fluid Mech*., 127, 473-496.
3. Arthurs, K.M., Moore, L.C., Peskin, C.S., Pitman, F.B. 1998 Modeling arteriolar flow and mass transport using the immersed boundary method. *J. Comput. Phys*. 147, 402.
4. Bertolotti, F. P., Herbert, T., and Spallart, P. R. 1992 Linear and nonlinear stability of the Blasius boundary layer. *J. Fluid Mech.* 242, 441-474.
5. Boiko, A.V., Grek, G.R., Dovgal, A.V., and Kozlov, V.V. 2002 *The Origin of Turbulence in Near-Wall Flows*. Springer.
6. Bons, J. P., Sondergarrd, R., and Rivir, R. B., 2001 Turbine Separation Control Using Pulsed Vortex Generator Jets, *Journal of Turbomachinery*, 123, 198-206
7. Casper, J., Lin, J.C., Yao, C.S. 2003 Effect of sub-boundary layer vortex generators on incident turbulence. *AIAA Paper* 2003-4162.
8. Coutanceau, M. and Bouard, R. 1977 Experimental determination of the main features of the viscous flow in a wake of a circular cylinder in uniform translation. Part 1. Steady flow. *J. Fluid Mech.* 79, 231-256.
9. Drazin, P.G. and Reid, W.H. 1981 *Hydrodynamic Stability*. Cambridge University Press.
10. Fornberg, B. 1980 A numerical study of steady viscous flow past a circular cylinder. *J. Fluid Mech.* 98, 819-855.
11. Gad-el_Hak, M. 2000 *Flow Control, Passive, Active, and Reactive Flow Management*, Cambridge University Press.
12. Godard, G., Stanislas, M. 2006 Control of a decelerating boundary layer. Part 1: Optimization of passive vortex generators. Aerospace Science and Technology 10, 181–191
13. Goldstein, D. Handler, R., Sirovich, L. 1995 Direct numerical simulation of the burbulent flow over a modeled riblet covered surface. *J. Fluid Mech.* 302, 333.
14. Greenblatt, D., Wygnanski, I. J. 2000 The control of flow separation by periodic excitation. *Progress in Aerospace Sciences* 36, 487-545
15. Grigoriadis, D.G.E., Bartzis, J.G., Goulas, A. 2003 LES of the flow past a rectangular

cylinder using the immersed boundary concept. *International Journal for Numerical Methods in Fluids*, 41(6), 615-632.

16. Hutchines, N., Choi, K-S. 2001 Experimental investigation of turbulence suppression by the imposition of a large-scale vortical control flow. *AIAA Paper* 2001-2775.
17. Jiang, L., Shan, H., Liu, C. 1999 Direct numerical simulation of boundary-layer receptivity for subsonic flow around airfoil. *Recent Advances in DNS and LES*, *Proceedings of the Second AFOSR (Air Force Office of Scientific Research) International Conference*, Rutgers, New Jersey, June 7-9.
18. Jiang, L. Shan, H., Liu, C., Visbal, M.R. 1999 Nonreflecting boundary conditions for DNS in curvilinear coordinates. *Recent Advances in DNS and LES*, *Proceedings of the Second AFOSR (Air Force Office of Scientific Research) International Conference*, Rutgers, New Jersey, June 7-9.
19. Jiang, L., Liu, C. 2003 Direct numerical simulation for flow separation control with pulsed jets. *AIAA Paper* 2003-0611.
20. Kerho, M., Kramer, B. 2003 Enhanced airfoil design incorporating boundary layer mixing devices. *AIAA Paper* 2003-0211.
21. Lin, J.C. 2002 Review of research on low-profile vortex generators to control boundary-layer separation. *Progress in Aerospace Sciences* 38, 389–420
22. Linnick, M., Fasel, H. 2003 A High-Order Immersed Boundary Method for Unsteady Incompressible Flow Calculations. *AIAA Paper* 2003-1124
23. Mittal, R., Iaccarino, G. 2005 Immersed boundary methods. *Annu. Rev. Fluid Mech.*, 37, 239-261
24. Mittal, R., Kotapati, R.B. 2005 Numerical study of resonant interactions and flow control in a canonical separated flow, *AIAA Paper* 2005-1261.
25. Nagib, H., Kiedaisch, J., Greenblatt, D., Wygnanski, I., Hassan, A., 2001 Effective flow control for rotorcraft applications at flight mach numbers, *AIAA Paper* 2001-2974.
26. Osborn, R.F., Kota, S., Geister, D., Lee, M., Tilmann, C. 2001 Active flow control using high frequency compliant structures. *AIAA Paper* 2001-4144.
27. Patel, M.P., Carver, R., Lisy, F.J., Prince, T.S., and Ng, T. 2002 Detection and control of flow separation using pressure sensors and miro-vortex generators. *AIAA Paper* 2002-0268.
28. Peskin, C.S. 1972 Flow patters around heart valves: a numerical method. *J. Comput. Phys*. 10, 252.
29. Saiki, E.M., Biringen, S. 1997 Spatial numerical simulation of boundary layer transition: effects of a spherical particle. *J. Fluid Mech.* 345, 133.
30. Schubauer, G.B., Spangenberg, W.G. 1960 Forced mixing in boundary layers. *J. Fluid Mech.* 8, 10-32.
31. Shan, H., Jiang, L., Liu, C. 2000 Numerical investigation of compressible separated flow around an NACA 0012 airfoil at 12° angle of attack. *Computational Fluid Dynamics Journal*, 9(2), 96-104.
32. Shan, H., Jiang, L., and Liu, C. 2005. Direct numerical simulation of flow separation

around a NACA 0012 Airfoil, *Computers and Fluids,* 34. 1096-1114

33. Shan, H., Jiang, L., Liu, C., Love, M, and Maines, B. 2005. Numerical simulation of time-dependent flow behind a pair of active vortex generators, *AIAA Paper* 2005-5018.
34. Shizawa, T., Mizusaki, Y. Response of time-depended flowfield structure behind an active vortex generators pair. *AIAA Paper* 2004-427.
35. Shizawa, T., Mizusaki, Y. Response of phase-averaged flowfield of longitudinal vortices to the height of active vortex generators pair. *AIAA Paper* 2005-4885.
36. Taylor, H.D. 1947 The elimination of diffuser separation by vortex generators. *United Aircraft Corporation Report No. R-4012-3*.
37. Yang, Z.Y. and Voke, P.R. 2001 Large-eddy simulation of boundary-layer separation and transition at a change of surface curvature. *J. Fluid Mech.* 439, 305-333.
38. Von Terzi, D.A., Linnick, M.N., Seidel, J., Fasel, H.F. 2001 Immersed boundary techniques for high-order finite difference methods, *AIAA Paper* 2001-2918.
39. Yarusevych, S., Kawall, J.G., Sullivan, P.E. 2003 Effect of acoustic excitation on airfoil performance at low Reynolds numbers. *AIAA J.* 41, 1599–1601.
40. Yarusevych, S., Sullivan, P.E., Kawall, J.G. 2005 Airfoil boundary layer separation and control at low Reynolds numbers. *Experiments in Fluids* 38: 545–547.
41. Yoon, S. and Kwak D. 1992 Implicit Navier-Stokes solver for three-dimensional compressible flows. *AIAA Journal* 30, 2653-2659.